

Ion Diffusion Velocity Measurements in a Multi-Ion-Species Plasma Shock

F. Chu,^{1,*} A. L. LaJoie,^{2,1} B. D. Keenan,¹ L. Webster,² S. J. Langendorf,¹ and M. A. Gilmore²

¹*Los Alamos National Laboratory, Los Alamos, New Mexico 87545, USA*

²*Department of Electrical and Computer Engineering,
University of New Mexico, Albuquerque, New Mexico 87131, USA*

(Dated: April 21, 2022)

Collisional plasma shocks generated from supersonic flows are an important feature in many astrophysical and laboratory high-energy-density plasmas. Compared to single-ion-species plasma shocks, plasma shock fronts with multiple ion species contain additional structure, including interspecies ion separation driven by gradients in species concentration, temperature, pressure, and electric potential. We present time-resolved density and temperature measurements of two ion species in collisional plasma shocks produced by head-on merging of supersonic plasma jets, allowing determination of the diffusion velocity of the ion species. Our results demonstrate that the lighter ion species diffuse faster than the heavier species within a shock front, consistent with predictions from the inter-ion-species transport theory. Results from the experiment approach quantitative agreement with theoretical prediction and 1D ion-Fokker-Planck kinetic simulation.

Introduction.—Shocks generated from supersonic flows are abundant in a variety of plasma environments, including astrophysical systems [1, 2] and high-energy-density (HED) laboratory experiments [3–6]. Compared to hydrodynamic shocks, plasma shocks may be governed primarily by Coulomb interactions between charged particles (collisional plasma shocks) [7] or by the influence of the electromagnetic fields (collisionless shocks) [8]. In addition, kinetic effects occurring in plasma shocks usually cannot be fully described using hydrodynamic shock theory and standard equation-of-state (EOS) models [9–12]. When multiple ion species are present in a collisional plasma shock, additional features can be introduced to the shock front structure, one of which is interspecies ion separation [13–16]. These effects have been studied in the context of inertial confinement fusion (ICF) experiments, in which mixtures of deuterium and tritium (DT) are compressed by strong shock waves to achieve fusion reactions. These shocks drive ion species separation through inter-ion-species diffusion [17], to the potential detriment of the fusion reactivity.

Work has been carried out to investigate multi-ion-species shocks and species separation in theory, simulation and experiment. A strong base of theoretical prediction is available on the diverse effects in multispecies plasma shocks: Kagan and Tang explored effects of electric field and temperature gradients on inter-ion-species transport [18, 19], Simakov *et al.* derived analytical solutions for weak planar shocks [11]. Furthermore ion-kinetic simulations provide a powerful capability to explore the physics, although understanding effects of dimensionality and treatment are not routine. Keenan *et al.* employed an ion-kinetic code to study collisional planar shocks in two-ion plasmas [20]. Comparatively few experiments have been performed that have been able to study the structure inside a collisional multi-ion-species plasma shock [16, 21–24].

In this Letter, we report the first detailed experimen-

tal investigation on the time evolution of the density and temperature of two separate ion species in a collisional plasma shock. The study demonstrates species separation between Ar and N ions within a plasma shock front and largely supports the prevailing inter-ion-species transport theory. We perform a 1D ion-Fokker-Planck (iFP) simulation, which is also in reasonable agreement with the experimental results.

Inter-Ion-Species Diffusion.—One can write $\rho \mathbf{u} = \sum_{\alpha} \rho_{\alpha} \mathbf{u}_{\alpha}$, where $\rho = \sum_{\alpha} \rho_{\alpha}$ is the total ion mass density and $\rho_{\alpha} = m_{\alpha} n_{\alpha}$ is the partial ion mass density of the species α (m_{α} and n_{α} are the mass and number density of the ion species α , respectively) [19]. Therefore, the diffusive ion mass flux of each species α in the center-of-mass frame of the plasma is given by $\mathbf{i}_{\alpha} = \rho_{\alpha} (\mathbf{u}_{\alpha} - \mathbf{u})$, where the total mass flux $\sum_{\alpha} \mathbf{i}_{\alpha} = 0$.

Applying mass conservation to species α and all ions, the flux \mathbf{i}_{α} is found to govern the mass concentration c_{α} of the species α through the continuity equation

$$\rho \frac{\partial c_{\alpha}}{\partial t} + \rho \mathbf{u} \cdot \nabla c_{\alpha} + \nabla \cdot \mathbf{i}_{\alpha} = 0, \quad (1)$$

where $c_{\alpha} = \rho_{\alpha} / \rho$. For a system containing only two ion species and close to local thermodynamic equilibrium, it is shown that the resulting flux has a linear relation with the thermodynamic forces [11, 16, 19]. The flux for the lighter ion species takes the form

$$\mathbf{i} = -\rho D \left(\nabla c + \frac{\kappa_p}{P_i} \nabla P_i + \frac{\kappa_{T_i}}{T_i} \nabla T_i + \frac{\kappa_{T_e}}{T_e} \nabla T_e + \frac{e \kappa_E}{T_i} \nabla \Phi \right), \quad (2)$$

with e the electron charge. The first term represents the classical diffusion flux resulting from the mass concentration gradient, and D is the classical diffusion coefficient. The remaining terms describe the baro-diffusion flux, ion and electron thermo-diffusion flux, and electro-diffusion

flux, driven by the respective gradients in total ion pressure P_i , ion temperature T_i , electron temperature T_e , and electrical potential Φ . Expressions for the solution of the respective diffusion coefficients D , κ_p , κ_{T_i} , κ_{T_e} , and κ_E , have been pursued using kinetic theory with concessions to a Maxwellian, and are listed in Refs. [11, 19]. Values for some of the coefficients are obtained in practice by numerical solution [16].

At the shock boundary, Eq. (2) predicts that all the diffusion flux terms for the lighter ion species point from the post-shock region to the pre-shock region except the relatively small electron thermo-diffusion flux, resulting in a net flux pointing in the same direction. Therefore, to satisfy the condition $\sum_{\alpha} \mathbf{i}_{\alpha} = 0$, the diffusion flux for the heavier ion species has to point in the opposite direction in the center-of-mass frame, causing the ion species to separate in the plasma shock [16].

Experiment.—To experimentally investigate species separation within a shock front, we create multi-ion-species plasma shocks by colliding two plasma jets head-on in a cylindrical vacuum chamber of 137 cm length and 76 cm diameter. The jets are produced by capacitor-driven plasma guns which accelerate plasma via $j \times B$ force [25, 26]. At the time when the plasma guns are fired, a gas puff consisting of 50% Ar and 50% N₂ by volume (58.8% Ar and 41.2% N₂ by mass concentration) is first pre-ionized in the gun nozzle and then accelerated into the vacuum chamber, to a speed of $v_{\text{jet}} = 18$ km/s. Each individual jet collides with an ion density $n_i \approx 5 \times 10^{14}$ cm⁻³, electron and ion temperature $T_i \approx T_e \approx 2$ eV, and mean charge $\bar{Z} \approx 1$ [16]. The Mach number is thus ~ 8.2 for Ar and ~ 4.9 for N in the pre-shock region.

The top view of the experimental setup is depicted in Fig. 1(a). A five-chord heterodyne interferometer is used to measure the time-resolved line-integrated electron density in the plasma shock [27, 28]. The laser emission is produced using a 320 mW, 561 nm solid state laser, which is divided into multiple lower-power beams and injected into the chamber through five single-mode fiber optic cables. Each probe beam is ~ 0.3 cm in diameter and placed horizontally in the midplane of the chamber at 0, 2, 4, 6, 8 cm with respect to the center. The first four probe beams are directed into the chamber perpendicularly to the side window (parallel with the shock front) while the fifth at an angle of 75° . These chord angles are chosen so that we can use chord 5 to measure the average electron density in the plasma shock and chords 1–4 to determine the bulk flow velocity in the post-shock region via time-of-flight analysis, as well as allow insight into the radial expansion of the post-shock plasma. After passing through the plasma, the probe beams are compared with a reference beam of the interferometer in the Mach-Zender configuration, and the line-integrated electron density is computed based on the relative phase shift [29].

As the density in our plasma shock is not high enough

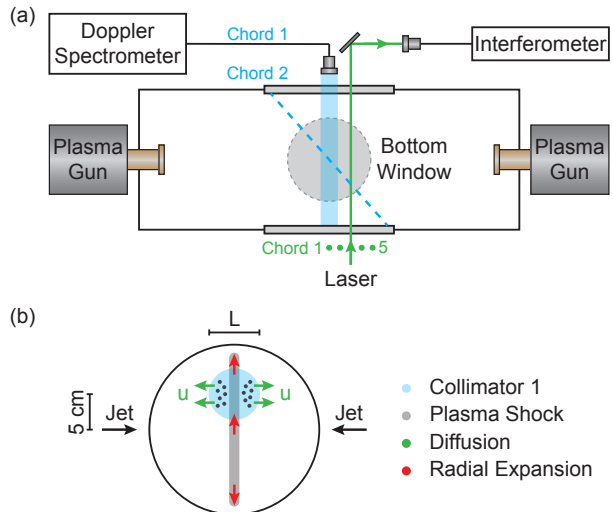


FIG. 1. (a) Schematic of the experimental setup. Plasma jets are generated by two plasma guns and head-on collide in the center of the chamber. The main diagnostics (not drawn to scale) include a two-chord Doppler spectrometer (colored in blue), a five-chord heterodyne interferometer (colored in green), a diagnostic spectrometer, and a fast intensified charge-coupled-device (ICCD) camera. All Doppler spectrometer and interferometer chords are in the horizontal midplane of the chamber except chord 1 of the former, which is placed at 5 cm above. (b) Schematic of the side window and chord 1 of the Doppler spectrometer, demonstrating that ion diffusion in the axial direction is the only major mechanism able to change the ion density in the collimator viewing volume. The diameter of the collimator $L=2$ cm.

for Stark broadening to be appreciable, Doppler broadening caused by ion thermal motion becomes the dominant source of spectral line broadening in the plasma [30]. A high-resolution spectrometer is utilized to measure the ion temperature in the shock through examining the width of the Doppler-broadened ion lines. The light emission from the plasma is collected using two collimators of $L = 2$ cm in diameter. Chord 1 is aligned with the central vertical plane of the chamber and held at 5 cm above the horizontal midplane, whereas chord 2 is in the vertical midplane but at an angle of $\sim 45^\circ$ with respect to the horizontal plane, as shown in Fig. 1. The light collected is then fielded by a double-pass high-resolution monochromator (McPherson 2062DP) with 2400 mm^{-1} grating, and the resulting spectrum is captured using a charge-coupled-device (CCD) camera (PCO Pixelfly). The ion temperature in our plasma shock is estimated based on the measured Doppler broadening of ArII 434.9 nm and NII 399.6 nm lines of Chord 2, which removes contributions to the broadening from the post-shock plasma radial expansion. In the experiment, we find that the width of the ion Doppler profile obtained from chord 1 is about 1.5 times as that obtained from chord 2 due to the plasma expansion in the radial direction, as shown in

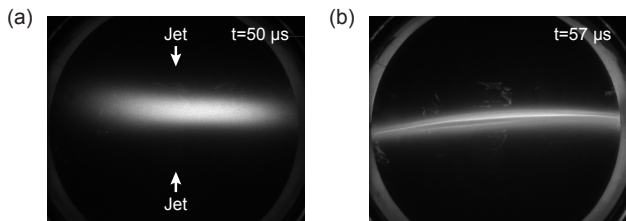


FIG. 2. (a)–(b) ICCD camera images of shock formation at 50 and 57 μs , respectively, as viewed through the bottom window shown in Fig. 1(a).

Fig. 3(d).

The ion emission spectrum is also used to infer the time-resolved density of each ion species in the plasma shock. For an atomic transition from an excited energy state to the lower state, the intensity of the emitted photons is proportional to the density of the excited state, a function strongly dependent on plasma parameters, such as the electron density and temperature [31]. In our case where the electron temperature stays about the same in the pre- and post-shock region, the density of the excited state can be assumed proportional to the total ion density to the zeroth-order approximation. The relative density of each ion species, therefore, can be inferred by monitoring the intensity of the Doppler-broadened spectral lines of each species.

Other diagnostics used in the experiment include a photodiode array at each gun nozzle to measure the jet velocity, a visible diagnostic spectrometer to interpret the electron temperature, and a fast intensified-CCD camera (PCO DiCam Pro) to image the shock formation. The diagnostic spectrometer records the broadband ion emission spectrum, which is then compared to PrismSPECT non-local-thermodynamic-equilibrium (non-LTE) modeling to infer the electron temperature in the plasma shock [16, 30, 32, 33].

Results.—The time evolution of multi-ion-species plasma jet merging captured by the ICCD camera is shown in Figs. 2(a) and 2(b). At 50 μs , the two jets are seen to reach the center of the chamber and about to collide. A sharp plasma shock front forms in several microseconds at 57 μs . Figure 3(a) shows an example of the broadband ion emission spectrum from the diagnostic spectrometer and a comparison to the PrismSPECT atomic modeling that we use to infer the electron temperature. Figure 3(c) shows an example of the Doppler broadened line, where the ion temperature is computed from performing deconvolution of instrumental broadening with the measured spectral profile. The experimentally inferred plasma parameters in the post-shock region are, electron temperature $T_e \approx 2.2$ eV, electron density $n_e \approx 1 \times 10^{15}$ cm^{-3} , Knudsen number ~ 0.4 , peak Ar temperature $T_{i-\text{Ar}} \approx 17$ eV, and peak N temperature

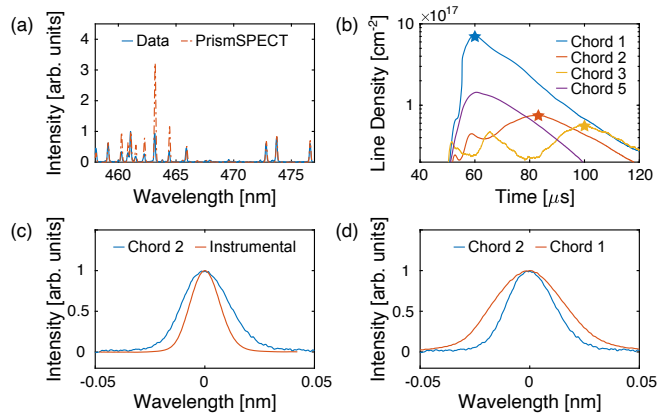


FIG. 3. (a) Example of broadband ion emission spectrum from the diagnostic spectrometer, along with the calculated spectrum using PrismSPECT at $T_e \approx 2.2$ eV. (b) Example of line-integrated electron density from interferometry. The peak line densities of chord 1, 2, and 3 are marked by stars, which are used in time-of-flight analysis to determine the plasma bulk flow velocity in post-shock region. (c) Example of Doppler-broadened ArII 434.9 nm line. The orange curve shows the instrumental broadening of the same line without the Doppler effects. (d) Comparison between Doppler-broadened ArII 434.9 nm lines obtained from chord 1 and 2 of Doppler spectroscopy. The center of profiles in (c) and (d) is shifted to 0 nm.

$T_{i-\text{N}} \approx 9.3$ eV.

One of the most important findings of this experiment is the observations of species separation within the plasma shock. Figure 4(a) shows the normalized density of Ar and N by the maximum values as a function of time, where the pre- and post-shock regions are separated by a blue dashed line. The density of both ion species increases at the same rate within errors at early time; however, at later time as the shock forms, the density of N ions decreases faster than that of Ar ions. This finding suggests that the lighter ion species (N) diffuse faster in the plasma shock gradients, consistent with the theoretical predictions. To bound the ion diffusion velocity, we consider the ion flow caused by plasma expansion and diffusion at the boundary of the collimator viewing volume shown in Fig. 1(b). In the radial direction, the ions enter and leave the volume, resulting in no net change of the ion density. Hence, the ion diffusion in the axial direction becomes the only major mechanism that decreases the ion density in the viewing volume. If we assume that the diffusion velocity u remains relatively constant shortly after the shock forms, then according to the continuity equation, the decrease of the normalized ion density should follow the exponential law $e^{-2ut/L}$, where the length scale L is the diameter of the collimator. By fitting the ion density in Fig. 4(a) from 58 to 65 μs , we find that the diffusion velocity for Ar and N is $u_{\text{Ar}} = (0.8 \pm 0.1) \times 10^3$ m/s and $u_{\text{N}} = (1.1 \pm 0.2) \times 10^3$ m/s, respectively. We

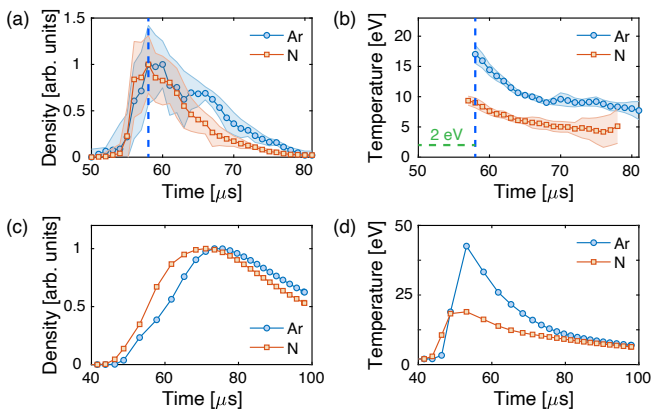


FIG. 4. (a) Measured ion density from chord 1 of the Doppler spectrometer as a function of time. The density is normalized by the peak value in each curve, marked by the blue vertical dashed line that separates the pre- and post-shock regions. (b) Measured ion temperature from chord 2 of the Doppler spectrometer as a function of time, demonstrating ion heating and temperature separation. The green horizontal dashed line represents ion temperature in the pre-shock region. (c) Simulated ion density as a function of time using the iFP code. The density is normalized by the peak value in each curve. (d) Simulated ion temperature as a function of time. The color bands in (a) and (b) indicate one-standard-deviation uncertainties.

also estimate the plasma bulk flow velocity in the post-shock region $u = \sum_{\alpha} c_{\alpha} u_{\alpha} \approx 920$ m/s, in agreement with the velocity of ~ 1100 m/s determined using time-of-flight analysis from the interferometry chords shown in Fig. 3(b). Thus, the diffusion velocity for Ar and N in the center-of-mass frame is $v_{\text{Ar}} = u_{\text{Ar}} - u \approx -120$ m/s and $v_{\text{N}} = u_{\text{N}} - u \approx 180$ m/s, with the relative diffusion velocity $\Delta v = v_{\text{N}} - v_{\text{Ar}} \approx 300$ m/s.

We evaluate the diffusion flux terms in Eq. (2) based on the experimental results to further understand their effects on species separation. The gradient of quantity Q is computed as $\nabla Q/Q \approx 2(Q_2 - Q_1)/L(Q_2 + Q_1)$, where the subscript 1 and 2 represent the pre- and post-shock region, respectively. We also assume that the initial concentration separation $\nabla c \approx 0$ for simplicity. The diffusion coefficients, calculated either analytically or numerically [16, 18, 19], are $D \approx 4.12$ m²/s, $\kappa_p \approx 0.28$, $\kappa_{T_i} \approx 0.28$, $\kappa_{T_e} \approx -0.06$, and $\kappa_E \approx 0.28$. Since the ambipolar electric field in Eq. (2) can be estimated as $\nabla \Phi = \nabla T_e/e$ [34], the contributions of each flux term to the diffusion

velocity of N ions in the center-of-mass frame are 233 m/s for baro-diffusion, 199 m/s for ion thermo-diffusion, -3 m/s for electron thermo-diffusion, and 4 m/s for electro-diffusion, with a total diffusion velocity $v_{\text{N}} \approx 400$ m/s. Similarly, the diffusion velocity for Ar in the center-of-mass frame is $v_{\text{Ar}} \approx -300$ m/s, resulting in a difference of ~ 700 m/s, relatively consistent with our experimental value. The above calculations suggest that both baro- and ion thermo-diffusions dominate over other diffusion terms, comparable to the mechanisms that drive species separation in ICF experiments [19].

We also experimentally measure heating of the distinct ion species. Figure 4(b) shows the time evolution of Ar and N ion temperature inferred from Doppler spectroscopy. Substantial ion heating and temperature separation are observed during the shock formation, with the temperature elevated from 2 eV to ~ 17 eV for Ar and to ~ 9 eV for N. Since the ion thermal energy is mainly transferred from its own kinetic energy, a ratio of ~ 2 in thermal energy gain is found between Ar and N as a result of their mass ratio (~ 2.9), indicating that some energy loss and equilibration occurring in the earliest collisions and formation time of the shock. Subsequent decrease of the ion temperature is observed due to classical thermal equilibration [30] among both ion species and electrons, with electrons radiatively cooling the plasma in the optically thin conditions.

A 1D Eulerian Vlasov-Fokker-Planck simulation is performed using the iFP code [20, 35, 36], as shown in Figs. 4(c)–4(d), to compare with the experimental results. The simulation in general agrees with the experimental data, successfully predicting a faster density decrease of N, ion heating, and temperature separation in the post-shock region shown in Figs. 4(a)–4(b). One of the noticeable discrepancies between the simulation and experiment is that the simulation predicts a higher ion temperature jump than the data. In the simulation, leading edge ions with a faster velocity reach the center of the chamber first and are heated to a high temperature, as shown in Fig. 4(d) at ~ 50 μ s. This effect can be easily seen in the simulation, but difficult to be observed in the experiment because of the low density of this ion group (Fig. 4(c) at ~ 50 μ s). In addition, the 1D simulation does not admit the possibility of radial expansion of the post-shock plasma, which is clearly seen in the experiment. This effect provides another mechanism by which kinetic energy is lost from the post-shock region, and contributes to the lower temperatures observed experimentally. It should be noted that the ion temperature separation demonstrated in Figs. 4(b) and 4(d) is a higher-order effect in deviations from LTE, whereas the diffusion flux theory assumes that all ion temperatures are equal [11]. Analyzing the simulation output, the average diffusion velocity for N and Ar in the center-of-mass frame is $v_{\text{N}} = 300$ m/s and $v_{\text{Ar}} = -260$ m/s, respectively. The total relative velocity is thus $\Delta v = 560$ m/s,

TABLE I. Comparison of the relative diffusion velocity for Ar and N in experiment, inter-ion-species diffusion theory, and iFP simulation. The relative diffusion velocity $\Delta v = v_{\text{N}} - v_{\text{Ar}}$.

Diffusion Velocity [m/s]	Experiment	Theory	Simulation
Δv	300 ± 200	700	560

in agreement with both of the experimental results and theoretical predictions. The comparison of the relative diffusion velocity for Ar and N in the experiment, theory, and simulation approaches described can be found in Table I.

Conclusions.—We present the first experimental study of the density and temperature evolution of Ar and N in collisional multi-ion-species plasma shocks. With measurements that resolve the diffusion velocity of each ion species, we demonstrate that the lighter species, in our case N, diffuse faster in a shock front, in agreement with theoretical understanding. The relative diffusion velocity is able to be calculated and found comparable with our experimental results. Furthermore, we find that significant ion heating occurs on the separate ion species during the formation of the shocks, with a temperature jump of ~ 15 eV for Ar and ~ 7 eV for N, similar to the initial distribution of jet kinetic energy but not simply proportional. We compare our experimental results with 1D Vlasov-Fokker-Planck simulation, and find that in general the calculation reproduces the experimental data, with differences that can be understood from the 3D geometry of the experimental plasma jets and shocks. This investigation on species separation in collisional plasma shocks provides useful new data to further understanding of multi-species plasma shocks and their relevance to HED/ICF configurations.

The authors would like to acknowledge T. Byvank and J. Dunn for valuable conversations and technical support. Research presented in this Letter was supported by the Laboratory Directed Research and Development program of Los Alamos National Laboratory under Project No. 20200564ECR. The plasma guns used in this work were designed and built by HyperJet Fusion Corporation under funding support of the Advanced Research Projects Agency–Energy (ARPA-E) of the U.S. Department of Energy (DOE) under Contract No. DE-AC5206NA25396 and cooperative agreement No. de-ar0000566.

* fchu@lanl.gov

- [1] D. Ryu, H. Kang, E. Hallman, and T. W. Jones, Cosmological Shock Waves and Their Role in the Large-Scale Structure of the Universe, *ApJ* **593**, 599 (2003).
- [2] A. Johlander, S. J. Schwartz, A. Vaivads, Y. V. Khotyaintsev, I. Gingell, I. B. Peng, S. Markidis, P.-A. Lindqvist, R. E. Ergun, G. T. Marklund, F. Plaschke, W. Magnes, R. J. Strangeway, C. T. Russell, H. Wei, R. B. Torbert, W. R. Paterson, D. J. Gershman, J. C. Dorelli, L. A. Avakov, B. Lavraud, Y. Saito, B. L. Giles, C. J. Pollock, and J. L. Burch, Rippled Quasiperpendicular Shock Observed by the Magnetospheric Multiscale Spacecraft, *Phys. Rev. Lett.* **117**, 165101 (2016).
- [3] B. A. Remington, High energy density laboratory astrophysics, *Plasma Phys. Control. Fusion* **47**, A191 (2005).
- [4] G. A. Rochau, J. E. Bailey, Y. Maron, G. A. Chandler, G. S. Dunham, D. V. Fisher, V. I. Fisher, R. W. Lemke, J. J. MacFarlane, K. J. Peterson, D. G. Schroen, S. A. Slutz, and E. Stambulchik, Radiating Shock Measurements in the Z-Pinch Dynamic Hohlraum, *Phys. Rev. Lett.* **100**, 125004 (2008).
- [5] R. P. Drake, Perspectives on high-energy-density physics, *Phys. Plasmas* **16**, 055501 (2009).
- [6] H. G. Rinderknecht, H.-S. Park, J. S. Ross, P. A. Amendt, D. P. Higginson, S. C. Wilks, D. Haberberger, J. Katz, D. H. Froula, N. M. Hoffman, G. Kagan, B. D. Keenan, and E. L. Vold, Highly Resolved Measurements of a Developing Strong Collisional Plasma Shock, *Phys. Rev. Lett.* **120**, 095001 (2018).
- [7] P. Hough, C. McLoughin, T. J. Kelly, P. Hayden, S. S. Harilal, J. P. Mosnier, and J. T. Costello, Electron and ion stagnation at the collision front between two laser produced plasmas, *J. Phys. D: Appl. Phys.* **42**, 055211 (2009).
- [8] R. L. Berger, J. R. Albritton, C. J. Randall, E. A. Williams, W. L. Kruer, A. B. Langdon, and C. J. Hanna, Stopping and thermalization of interpenetrating plasma streams, *Phys. Fluids B Plasma Phys.* **3**, 3 (1991).
- [9] M. J. Rosenberg, H. G. Rinderknecht, N. M. Hoffman, P. A. Amendt, S. Atzeni, A. B. Zylstra, C. K. Li, F. H. Séguin, H. Sio, M. G. Johnson, J. A. Frenje, R. D. Petrasso, V. Y. Glebov, C. Stoeckl, W. Seka, F. J. Marshall, J. A. Delettrez, T. C. Sangster, R. Betti, V. N. Goncharov, D. D. Meyerhofer, S. Skupsky, C. Bellei, J. Pino, S. C. Wilks, G. Kagan, K. Molvig, and A. Nikroo, Exploration of the Transition from the Hydrodynamiclike to the Strongly Kinetic Regime in Shock-Driven Implosions, *Phys. Rev. Lett.* **112**, 185001 (2014).
- [10] G. Kagan, D. Svyatskiy, H. G. Rinderknecht, M. J. Rosenberg, A. B. Zylstra, C.-K. Huang, and C. J. McDewitt, Self-Similar Structure and Experimental Signatures of Suprathermal Ion Distribution in Inertial Confinement Fusion Implosions, *Phys. Rev. Lett.* **115**, 105002 (2015).
- [11] A. N. Simakov, B. D. Keenan, W. T. Taitano, and L. Chacón, Plasma ion stratification by weak planar shocks, *Phys. Plasmas* **24**, 092702 (2017).
- [12] S. Zhang and S. X. Hu, Species Separation and Hydrogen Streaming upon Shock Release from Polystyrene under Inertial Confinement Fusion Conditions, *Phys. Rev. Lett.* **125**, 105001 (2020).
- [13] P. Amendt, O. L. Landen, H. F. Robey, C. K. Li, and R. D. Petrasso, Plasma Barodiffusion in Inertial-Confinement-Fusion Implosions: Application to Observed Yield Anomalies in Thermonuclear Fuel Mixtures, *Phys. Rev. Lett.* **105**, 115005 (2010).
- [14] C. Bellei, P. A. Amendt, S. C. Wilks, M. G. Haines, D. T. Casey, C. K. Li, R. Petrasso, and D. R. Welch, Species separation in inertial confinement fusion fuels, *Phys. Plasmas* **20**, 012701 (2013).
- [15] E. Vold, R. Rauenzahn, and A. N. Simakov, Multi-species plasma transport in 1D direct-drive ICF simulations, *Phys. Plasmas* **26**, 032706 (2019).
- [16] T. Byvank, S. J. Langendorf, C. Thoma, and S. C. Hsu, Observation of shock-front separation in multi-ion-species collisional plasma shocks, *Phys. Plasmas* **27**, 042302 (2020).
- [17] G. Kagan, S. D. Baalrud, and J. Daligault, Influence of coupling on thermal forces and dynamic friction in plasmas with multiple ion species, *Phys. Plasmas* **24**, 072705 (2017).

- [18] G. Kagan and X.-Z. Tang, Electro-diffusion in a plasma with two ion species, *Phys. Plasmas* **19**, 082709 (2012).
- [19] G. Kagan and X.-Z. Tang, Thermo-diffusion in inertially confined plasmas, *Physics Letters A* **378**, 1531 (2014).
- [20] B. D. Keenan, A. N. Simakov, W. T. Taitano, and L. Chacón, Ion species stratification within strong shocks in two-ion plasmas, *Phys. Plasmas* **25**, 032103 (2018).
- [21] H. G. Rinderknecht, M. J. Rosenberg, C. K. Li, N. M. Hoffman, G. Kagan, A. B. Zylstra, H. Sio, J. A. Frenje, M. Gatu Johnson, F. H. Séguin, R. D. Petrasso, P. Amendt, C. Bellei, S. Wilks, J. Delettrez, V. Y. Glebov, C. Stoeckl, T. C. Sangster, D. D. Meyerhofer, and A. Nikroo, Ion Thermal Decoupling and Species Separation in Shock-Driven Implosions, *Phys. Rev. Lett.* **114**, 025001 (2015).
- [22] S. C. Hsu, T. R. Joshi, P. Hakel, E. L. Vold, M. J. Schmitt, N. M. Hoffman, R. M. Rauenzahn, G. Kagan, X.-Z. Tang, R. C. Mancini, Y. Kim, and H. W. Herrmann, Observation of interspecies ion separation in inertial-confinement-fusion implosions, *EPL* **115**, 65001 (2016).
- [23] H. G. Rinderknecht, H.-S. Park, J. S. Ross, P. A. Amendt, S. C. Wilks, J. Katz, N. M. Hoffman, G. Kagan, E. L. Vold, B. D. Keenan, A. N. Simakov, and L. Chacón, Measurements of ion velocity separation and ionization in multi-species plasma shocks, *Phys. Plasmas* **25**, 056312 (2018).
- [24] T. R. Joshi, S. C. Hsu, P. Hakel, N. M. Hoffman, H. Sio, and R. C. Mancini, Progress on observations of interspecies ion separation in inertial-confinement-fusion implosions via imaging x-ray spectroscopy, *Phys. Plasmas* **26**, 062702 (2019).
- [25] S. C. Hsu, S. J. Langendorf, K. C. Yates, J. P. Dunn, S. Brockington, A. Case, E. Cruz, F. D. Witherspoon, M. A. Gilmore, J. T. Cassibry, R. Samulyak, P. Stoltz, K. Schillo, W. Shih, K. Beckwith, and Y. C. F. Thio, Experiment to Form and Characterize a Section of a Spherically Imploding Plasma Liner, *IEEE Trans. Plasma Sci.* **46**, 1951 (2018).
- [26] Y. C. F. Thio, S. C. Hsu, F. D. Witherspoon, E. Cruz, A. Case, S. Langendorf, K. Yates, J. Dunn, J. Cassibry, R. Samulyak, P. Stoltz, S. J. Brockington, A. Williams, M. Luna, R. Becker, and A. Cook, Plasma-Jet-Driven Magneto-Inertial Fusion, *Fusion Sci. Technol.* **75**, 581 (2019).
- [27] E. C. Merritt, A. G. Lynn, M. A. Gilmore, and S. C. Hsu, Multi-chord fiber-coupled interferometer with a long coherence length laser, *Rev. Sci. Instrum.* **83**, 033506 (2012).
- [28] E. C. Merritt, A. G. Lynn, M. A. Gilmore, C. Thoma, J. Loverich, and S. C. Hsu, Multi-chord fiber-coupled interferometry of supersonic plasma jets (invited), *Rev. Sci. Instrum.* **83**, 10D523 (2012).
- [29] I. H. Hutchinson, *Principles of Plasma Diagnostics*, 2nd ed. (Cambridge University Press, Cambridge, 2002).
- [30] S. J. Langendorf, K. C. Yates, S. C. Hsu, C. Thoma, and M. Gilmore, Experimental Measurements of Ion Heating in Collisional Plasma Shocks and Interpenetrating Supersonic Plasma Flows, *Phys. Rev. Lett.* **121**, 185001 (2018).
- [31] U. Fantz, Basics of plasma spectroscopy, *Plasma Sources Sci. Technol.* **15**, S137 (2006).
- [32] S. C. Hsu, E. C. Merritt, A. L. Moser, T. J. Awe, S. J. E. Brockington, J. S. Davis, C. S. Adams, A. Case, J. T. Cassibry, J. P. Dunn, M. A. Gilmore, A. G. Lynn, S. J. Messer, and F. D. Witherspoon, Experimental characterization of railgun-driven supersonic plasma jets motivated by high energy density physics applications, *Phys. Plasmas* **19**, 123514 (2012).
- [33] E. C. Merritt, A. L. Moser, S. C. Hsu, J. Loverich, and M. Gilmore, Experimental Characterization of the Stagnation Layer between Two Obliquely Merging Supersonic Plasma Jets, *Phys. Rev. Lett.* **111**, 085003 (2013).
- [34] X.-Z. Tang, H. L. Berk, Z. Guo, and C. J. McDevitt, Reduced Fokker-Planck models for fast particle distribution across a transition layer of disparate plasma temperatures, *Phys. Plasmas* **21**, 032707 (2014).
- [35] B. D. Keenan, W. T. Taitano, A. N. Simakov, L. Chacón, and B. J. Albright, Shock-driven kinetic and diffusive mix in high-Z pusher ICF designs, *Phys. Plasmas* **27**, 022704 (2020).
- [36] W. T. Taitano, B. D. Keenan, L. Chacón, S. E. Anderson, H. R. Hammer, and A. N. Simakov, An Eulerian Vlasov-Fokker-Planck algorithm for spherical implosion simulations of inertial confinement fusion capsules, *Computer Physics Communications* **263**, 107861 (2021).